IEEE Robotics and Automation Letters (RAL) paper presented at
2024 IEEE/RSJ International Conference on Intelligent Robots and Systems (IROS)
October 14-18, 2024. Abu Dhabi, UAE

# Origami-Inspired Wearable Robot for Shoulder Abduction Assistance: A Double-Petal Mechanism Utilizing Shape Memory Alloy Actuators

Chongyoung Chung, Kyujin Hyeon, Jaeyeon Jeong, Dae-Young Lee, *Member, IEEE*, and Ki-Uk Kyung*, *Member, IEEE*

***Abstract*— This paper proposes a novel wearable robot designed to assist with shoulder abduction using a double-petal mechanism based on petal fold origami driven by shape memory alloy (SMA)-based artificial muscle. The proposed double-petal mechanism consists of two petal structures that mimic the scapula and humerus, respectively. It follows the scapulohumeral rhythm to prevent bone collision and reduce the compressive force on the glenohumeral joint. The mechanism is designed to achieve high mechanical advantage and torque output while minimizing the overall weight using lightweight SMA spring actuators and carbon fiber-reinforced plastic-based frames. The proposed robot can assist with shoulder abduction both with (active support) and without energy input (passive support) using bundles of SMA spring actuators. It can generate assistance torque up to 6.36 Nm passively and 12.6 Nm actively at a 90° abduction angle. To verify the assistance performance of the proposed robot, surface electromyography of the lateral deltoid is measured during shoulder abduction with and without the assistance of the robot and the results confirm that the robot effectively assists in shoulder abduction.**

## I. Introduction

Shoulder abduction is one of the most frequently used and important movements of the upper limbs in various fields such as the manufacturing industry, assisting in the activities of daily living (ADL), and rehabilitation or treatment [1]-[12]. For example, workers in manufacturing industries frequently use shoulder abduction for lifting heavy weights or working on overhead tasks, which can lead to musculoskeletal disorders [6], [12]. Additionally, rehabilitation of spasticity and shoulder subluxation due to muscle weakness following shoulder abduction are challenging problems for neurological disability patients in the rehabilitation field.

This work was supported in part by the R&D Program (No. 2022R1A2B5B02002074) of the National Research Foundation (NRF), Korea, and in part by the Translation Research Program for Rehabilitation Robots (NRCTR-EX21002), National Rehabilitation Center, Ministry of Health and Welfare, Korea. (Corresponding author: Ki-Uk Kyung.)

Chongyoung Chung, Kyujin Hyeon, Jaeyeon Jeong, and Ki-Uk Kyung are with the Department of Mechanical Engineering, Korea Advanced Institute of Science and Technology, Daejeon 34141, South Korea (e-mail: cy.chung@kaist.ac.kr; axz0502@kaist.ac.kr; jjy7583@kaist.ac.kr; kyungku@kaist.ac.kr).

Dae-Young Lee is with the Department of Aerospace Engineering, Korea Advanced Institute of Science and Technology, Daejeon 34141, South Korea (e-mail: ae_dylee@kaist.ac.kr).

This work involved human subjects or animals in its research. Approval of all ethics and experimental procedures and protocols was granted by the Institutional Review Board at the Korea Advanced Institute of Science and Technology (KH2021-195).



Wearable robots designed for shoulder abduction can provide assistance to workers and patients based on individual needs. However, if these wearable robots lack portability, being heavy and bulky, it could pose difficulties in their practical use in ADL, even if they exhibit powerful performance. Additionally, as wearable robots synchronize their movements with the upper limb of the users, it is crucial for them to prioritize safety and provide sufficient assistance without imposing undesired or misaligned load to the body. They should accurately deliver assistance force or torque in the appropriate direction, considering human musculoskeletal biomechanics. For example, if excessive compressive force, perpendicular to shoulder abduction direction, is applied to the glenohumeral (GH) joint during shoulder abduction assistance, it can lead to rotator cuff tear problem due to the friction between the rotator cuff and acromion [13], [14]. Furthermore, it should consider the trajectory of scapulohumeral rhythm (SHR), which involves coordinated rotation between scapula and humerus with a ratio of 1:2, to avoid bone collision issues in the shoulder joint [3].

Over the past few decades, several wearable robots for assisting shoulder abduction have been widely developed, and it can be classified into three types: Type I. pulling the arm over the shoulder using contraction and linear actuator such as tendon-driven actuator (direct contraction type over the shoulder) [1]-[3], Type II. Lifting up the arm driven by volumetric expansion with pneumatic pressure at the armpit (volume expansion type at the armpit) [4]-[6], and Type III. Lifting up the shoulder by supporting abduction torque driven by motor-link mechanism (exoskeleton type) [7]-[9]. The direct contraction type uses the tendon-driven mechanism which has lightweight and good portability with a compact design. However, as the contraction force is parallel to the upper limb, it can irritate the skin and slip on the skin [3], [11]. Also, it is difficult to contract at a large angle with the upper limb using a direct contraction, because it produces a large compressive force to the GH joint occur [1]. Since it is structurally difficult to make it follow the SHR, a method of using four-bar-linkage structures has been proposed, but the linkage structure spreads widely over the shoulder as the abduction angle increases, which can increase the volume [3].

In the case of the volume expansion type, they use a pneumatic actuator composed of a powerful air compressor and a deformable bladder. This type shows great advantages in a range of motion (ROM) and small compressive force. Also, intrinsic compliance of the bladder makes advantages in following SHR without additional mechanisms [6]. However, the air compressor to create pressure is heavy and consumes a lot of energy, resulting in disadvantages for portability. Also,

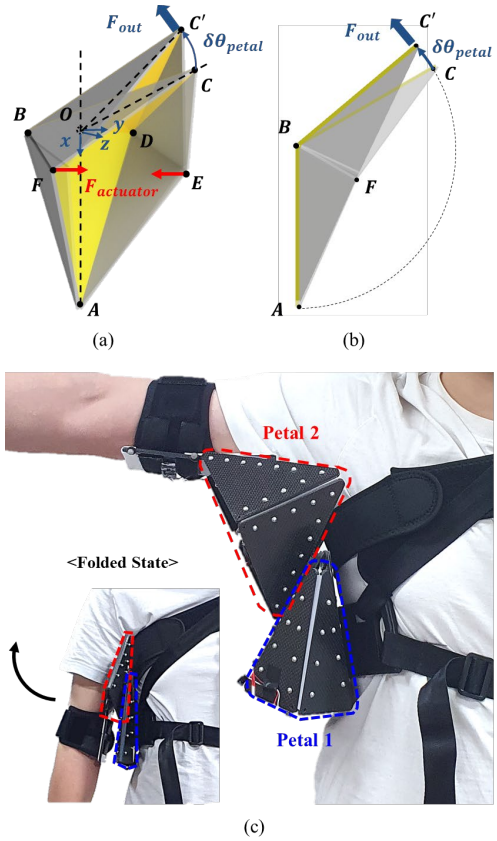


Fig. 1. (a) Diagonal and (b) side view of the working principle of a single petal mechanism. When actuator contracted, the mechanism is straightening the bending and unfolding. (c) Proposed robot uses a double-petal mechanism which is composed of petal 1 and 2, which assists the shoulder abduction while the actuator contracted.

due to the compliance of the bladder, the applied force to the user can be transferred in misdirection [11]. On the other hand, the exoskeleton type shows high performance of the torque output and ROM because the powerful motor-gear system directly rotates each joint. However, these robots are heavy and bulky due to the heavy components such as motors, gears, and frames [7]-[9], [14]. Particularly, in this type, not only is a complex link design required to follow the SHR trajectory, but the controllability is also significantly compromised. Therefore, a new type of assistance mechanism is necessary for shoulder abduction with small and lightweight design, sufficient performance, and safe interaction.

We propose a novel mechanism based on origami with shape memory alloy (SMA) actuators for assisting shoulder abduction. Origami, which consists of rigid membrane and soft hinges, has versatile shape-changing ability, allowing for significant expansion with initially compact design [15]. Especially, we propose a petal mechanism, which is inspired by petal fold origami as shown in Fig. 1 (a) and (b). The working principle of the petal mechanism is same as petal fold origami; the two ends of the actuator is placed at E and F, and the structure is expanded and produced pushing force ($\angle AOC \uparrow$) when the actuator contracts and produces contraction force ($\overline{EF} \downarrow$). One of the main advantages of the petal mechanism is a small compressive force generation. This mechanism cannot induce compressive force in the rotation axis ($\overline{BD}$) because the rotation axis and the direction of the actuator force ($\overline{EF}$) are parallel. Another advantage is a high mechanical advantage (MA) owing to the scissors mechanism structure (□AECF) inside the petal mechanism as shown in Fig. 1 (a). [16], [17]. The high MA of the petal mechanism enables a small input force to produce a large output force, resulting in a significant torque output. This makes it advantageous for creating high torque output with a small amount of input force.

Shape memory alloy (SMA) actuators are one of the great candidates for use as a contractive and linear actuator to work with the petal mechanism. SMA actuators produce force and deformation through a phase transition between martensite and austenite phases induced by temperature change [18]-[25]. This actuator shows good performances such as high force output due to the high-power density [26], [27]. However, since the wire geometry-based SMA actuator shows a high power-to-weight ratio (> 50 W/g), they are limited to low levels of strain (< 5 %) [22], [23]. Therefore, the spring geometry-based SMA actuator, known as the SMA spring actuator, was chosen for the proposed mechanism to improve the strain (> 200 %). Additionally, since the SMA spring actuator can generate a restoring force without energy input, it enables energy-efficient assistance of shoulder abduction without a current input. Furthermore, this actuator geometry contracts on its own, making it beneficial for directly contracting the petal mechanism without tendon. The utilization of petal origami and SMA actuator in a mechanism can solve the challenges due to not only the compact design and high MA properties of the origami structure but also high power-to-weight ratio and restoring force properties of SMA actuators.

In this paper, we propose a new wearable robot using an origami-based petal mechanism to assist shoulder abduction driven by SMA actuators. To mimic the SHR of the scapula and humerus during shoulder abduction, the double-petal mechanism using two petal mechanisms is used. This mechanism not only reduces the misalignment problem by following SHR trajectory and compressive force to the GH joint, but it also decreases the required force input due to the high MA property. Then, an optimization process is conducted to decide the geometry of the petal mechanism and specifications of the SMA spring actuator. Finally, the wearable robot using the proposed mechanism and actuators was designed as shown in Fig. 1 (c). The performance of the proposed robot was evaluated through user tests with a group of ten healthy men, with the results demonstrating sufficient assistance performance for every subject.

## II. Design Process of the Mechanism for Assisting Shoulder Abduction

### A. Mechanism Design

Prior to the mechanism design, the SHR during shoulder abduction was examined as shown in Fig. 2 (a). The SHR can be simply modeled as two triangles with a variable dislocation length ($l_d$) as the abduction angle. And an instantaneous rotation center (IRC) of SHR is the intersection point of each rotated scapula and humerus axis. Therefore, proposed mechanism is modeled as a double-petal mechanism composed of two petal mechanisms with constant dislocation

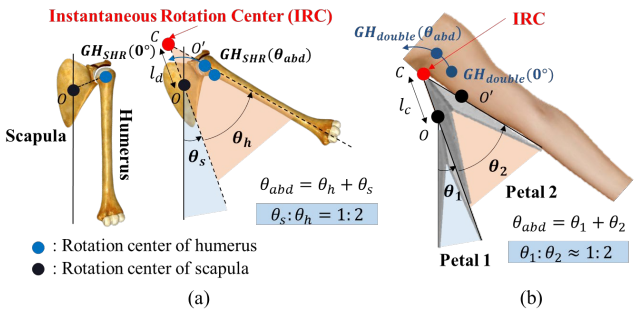


Fig. 2. Instantaneous rotation center (IRC) of (a) the following SHR and (b) double-petal mechanism. The double-petal mechanism mimics the scapula and humerus, and especially the IRC.

length ($l_c$) to follow the SHR as shown in Fig. 2 (b). To minimize the misalignment error of the GH joint between SHR and the double-petal mechanism, the objective function is defined as (1). And the objective function was simulated to find optimized $l_c$ using each GH joint trajectory model as (2) and (3) and 70 mm was selected as $l_c$. The $R(\theta)$ in (1)-(3) means that the rotation matrix rotates about $\theta$ in a plane.

$$err(\theta_{abd}) = \|GH_{SHR}(\theta_{abd}) - GH_{double}(\theta_{abd})\| \quad (1)$$

$$\overrightarrow{GH}_{SHR}(\theta_{abd}) = R(\theta_s)\cdot\overrightarrow{GH}_{SHR}(0°) = R(\frac{\theta_{abd}}{3})\cdot\overrightarrow{GH}_{SHR}(0°) \quad (2)$$

$$\begin{aligned}\overrightarrow{GH}_{double}(\theta_{abd}) &= \overrightarrow{OC}(\theta_1) + \overrightarrow{C,GH}_{double}(\theta_{abd}) \\ &= R\left(\frac{\theta_{abd}}{3}\right)\cdot\overrightarrow{OC}(0°) + R(\theta_{abd})\cdot\overrightarrow{C,GH}_{double}(0°)\end{aligned} \quad (3)$$

Then, the geometries of the double-petal mechanism are optimized to maximize the MA and maintain the angle ratio ($= \theta_2/\theta_1$) of 2, where $\theta_1$ and $\theta_2$ are the rotation angles of petal 1 and 2, respectively. The development figures of each petal mechanism are shown in Fig. 3 (a). To prevent the collision between the upper body and the mechanism ($\triangle OO'C$ in Fig. 2 (b)), the central parts of petal 2 were removed. Then, rectangle parts were added with reverse folding to increase the structural stability.

The value of $\alpha_i$ and $\beta_i$ determine the maximum rotation angle ($\theta_{max,i}$). The relationship between $\alpha_i$ and $\beta_i$ can be calculated as (4) using the parallel property of $\overrightarrow{AG}//\overrightarrow{CG}$ when petal rotates $\theta_{max}$ as shown in Fig. 3 (a) in 3D space. Therefore, $\beta_i$ can be expressed as a function of $\alpha_i$ and $\theta_{max}$.

$$\beta_i = sin^{-1}\left(sin\alpha_i \cdot sin\frac{\theta_{max,i}}{2}\right) = f(\alpha_i, \theta_{max,i}) \quad (4)$$

Since the petal 1 and 2 are needed to limit the rotation only up to $60°$ ($0° \le \theta_1 \le 60°$) and $120°$ ($0° \le \theta_2 \le 120°$), respectively, $\beta_1$ and $\beta_2$ can be calculated as (5) and (6).

$$\beta_1 = sin^{-1}\left(sin\alpha_1 \cdot sin\frac{\theta_{max,1}}{2}\right) = sin^{-1}\left(\frac{sin\alpha_1}{2}\right) \quad (5)$$

$$\beta_2 = sin^{-1}\left(sin\alpha_2 \cdot sin\frac{\theta_{max,2}}{2}\right) = sin^{-1}\left(\frac{\sqrt{3}}{2}sin\alpha_2\right) \quad (6)$$

Also, the value of $\alpha_i$ and $\beta_i$ determine the MA of petal mechanism using the orthogonality of $\overrightarrow{AG}\cdot\overrightarrow{CG} = 0$ as (7). Therefore, the mechanical advantage can be finally expressed as a function of $\alpha_i$ and $\theta_{petal}$ as (8) where $\theta_{\angle GBE}$ is an angle of $\angle GBE$ when the development figures are folded in 3D space.

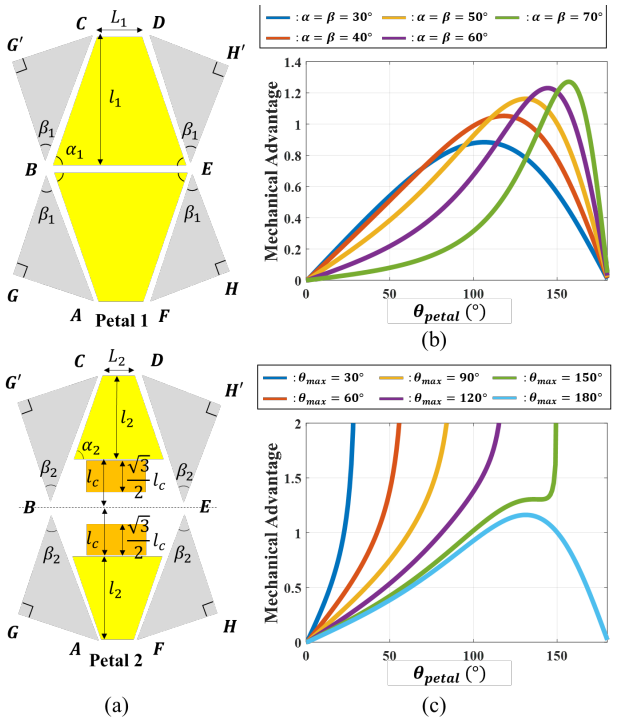


Fig. 3. (a) Development figures of petal 1 and petal 2. (b) The mechanical advantage relationships about (b) $\alpha(=\beta)$ (c) and $\theta_{max}$ when $\alpha = 50°$.

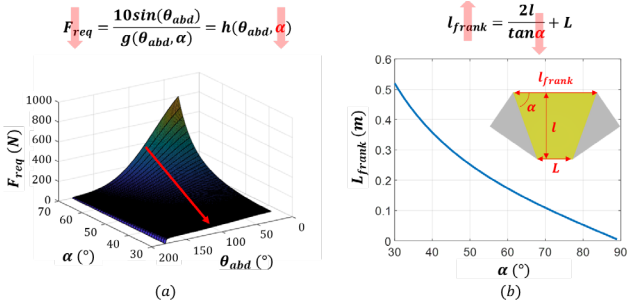


Fig. 4. The trade-off relationships of the (a) required force to each petal mechanism and (b) the overall frank length. Both required force and frank length should be minimized.

$$cos(\theta_{\angle GBE}) + tan(\alpha_i)\cdot cos(\frac{\theta_{petal}}{2})\cdot sin(\theta_{\angle GBE}) = \frac{cos(\beta_i)}{cos(\alpha_i)} \quad (7)$$

$$\begin{aligned}MA = \frac{F_{out}}{F_{in}} &= -\frac{\delta\overline{EF}}{\delta\overline{AOC}} = -\frac{2cos(\beta_i)}{sin(\alpha_i)}\cdot\frac{dcos(\theta_{\angle GBE})}{d\theta_{petal}} \\ &= f(\alpha_i, \theta_{petal})\end{aligned} \quad (8)$$

Fig. 3. (b) and (c) show the MA properties related to $\alpha_i$, $\beta_i$, and $\theta_{petal,i}$. If $\alpha_i = \beta_i$, which means that $\theta_{max,i} = 180°$, the MA is increased as the $\alpha_i$ increases. If $\theta_{max,i}$ is changed to a value lower than 180° such as 120°, the MA trends change about the same $\alpha$ as shown in Fig. 3 (c). The double-petal mechanism should maintain the angle ratio of 2 to mimic the SHR, which means that the torque output of each petal should same when the angle ratio is maintained as 2. If $\alpha_1$ and $\alpha_2$ are the same as $\alpha$, the force output ($F_{out,i}$) are the same when the same force input ($F_{actuator,i}$) are exerted on each petal while the $\theta_1 : \theta_2 = 1:2$ as shown in Fig. 3 (c). Also, if $l_1$ and $l_2 + l_c$ are the same as $l$, the torque output will be also the same

TABLE I. Design Parameters of the SMA spring actuator

| Parameter | Value | |
|---|---|---|
| | Petal 1 | Petal 2 |
| Wire diameter (d) | 0.5 mm | 0.5 mm |
| Coil outer diameter (D) | 2.0 mm | 2.0 mm |
| Number of turns (n) | 40 | 100 |
| Number of coils (N) | 10 | 10 |
| Transition temperature ($A_s$) | 26.4 ℃ | 26.4 ℃ |

because the moment arm ($T_i$) are the same as (9)-(11). Then, using these properties, mechanism was optimized to maximize the MA at 90° abduction angle.

$$T_1 = l_1 \cdot F_{out,1} = l_1 \cdot F_{actuator,1} \cdot MA(\alpha_1, \theta_1) \quad (9)$$

$$T_2 = (l_2 + l_c) \cdot F_{out,2} = (l_2 + l_c) \cdot F_{actuator,2} \cdot MA(\alpha_2, \theta_2) \quad (10)$$

$$T_1(l, \alpha, \theta_1) = T_2(l, \alpha, \theta_2) \quad where\ \theta_2 = 2\theta_1 \quad (11)$$

### B. Mechanism Optimization

In the case of $l$, the larger the moment arm is better for producing torque output. However, if it is longer than the length of the upper arm, it may interfere with the movement of other joints, so it is assumed as 150 mm to match the length of the upper arm [28]. Next, $\alpha$ is a variable that determines the MA, that is, the torque that develops as (9)-(11). To determine $\alpha$, the required force ($F_{req}$) to be applied to achieve target torque through the actuator to the proposed mechanism was obtained, which is the same as the graph shown in Fig. 4 (a). The force to be applied through the actuator decreases as $\alpha$ decreases. However, if the $\alpha$ becomes smaller, the length of the axis of rotation of the petal located in the armpit ($L_{frank}$) increases. An increase in $L_{frank}$ means an increase in the size of the overall structure, thus creating a trade-off relationship with the required force. To optimize the two values, we multiplied each other to create an objective function ($f_{obj}$) and simulated to minimize: $f_{obj} = F_{req} \times L_{frank}$. The results show that the objective function is optimized at $\alpha = 52°$. Then, the $\beta_1$ and $\beta_2$ can be calculated using equations (4) and (5) as 23° and 43°, respectively. Based on this result, it was possible to calculate the force that the actuator should generate, and it was determined that it should be capable of generating up to 200 N of force.

### C. Fabrication Process of the Mechanism

Fig. 5. shows a fabrication process of the proposed mechanism. First, the base frame is fabricated using 2 mm thickness carbon fiber-reinforced plastic (CFRP) by a CNC machine following the optimized design in the previous section. Due to its high elastic modulus (100~200 GPa) and low density (1500~2100 kg/m$^3$) compared to metallic alloys, CFRP can be used to fabricate lightweight and strong frames. A hinge is also necessary to connect each base frame. There are two types of hinge structures: a rigid (metal) hinge and a soft hinge. However, the soft hinge is more suitable for the mechanism due to the high friction, misalignment, and stress concentration issues associated with the rigid hinge [29]. The soft hinge is composed of a composite layer with PET film (0.1mm) and nylon cloth and it is fabricated using a laser cutter.

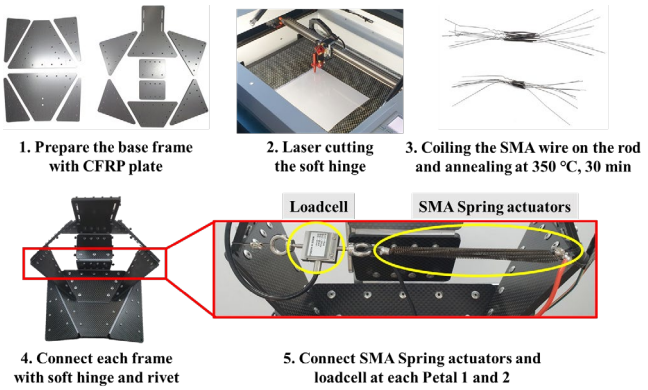


Fig. 5. Fabrication process of the proposed mechanism.

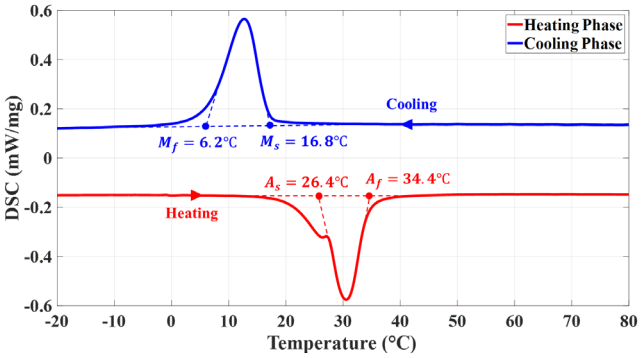


Fig. 6. DSC results of the SMA wire.

Then, the artificial muscles using SMA spring actuators were designed. To maximize the restoring force, the slightly higher transition temperature ($A_s$) from the martensite to austenite than the room temperature was selected. The transition temperature of the SMA wire was confirmed through a differential scanning calorimetry (DSC), and the results are presented in Fig. 6. The SMA was heated and cooled between -20℃ to 80℃ at a constant rate of 5℃/min, and $A_s$ was measured about 26.4℃. And the bundles of SMA spring actuators were used to achieve a force output greater than 200 N. Then, the design parameters of the SMA spring actuator can be determined as shown in Table I.

The SMA wire is coiled on the rod and annealed for 30 mins at 350℃ in an oven and then quenched in cold water. After preparing the materials such as base frames, soft hinges, and SMA spring actuators, the frames were connected with soft hinges using rivets [30]. Finally, the SMA spring actuators and loadcell (Dacell, UU74) were respectively connected to the end of each petal structure. The loadcell will be used to control the actuator by measuring the force generated.

### D. Performance of the Mechanism

After optimization and fabrication of the proposed mechanism, performance evaluation was conducted to validate the theoretical data. For the proposed mechanism, two aspects were considered mainly for validation: a comparison of the torque output between theoretical and experimental data, and maintenance of angle ratio between two petal mechanisms

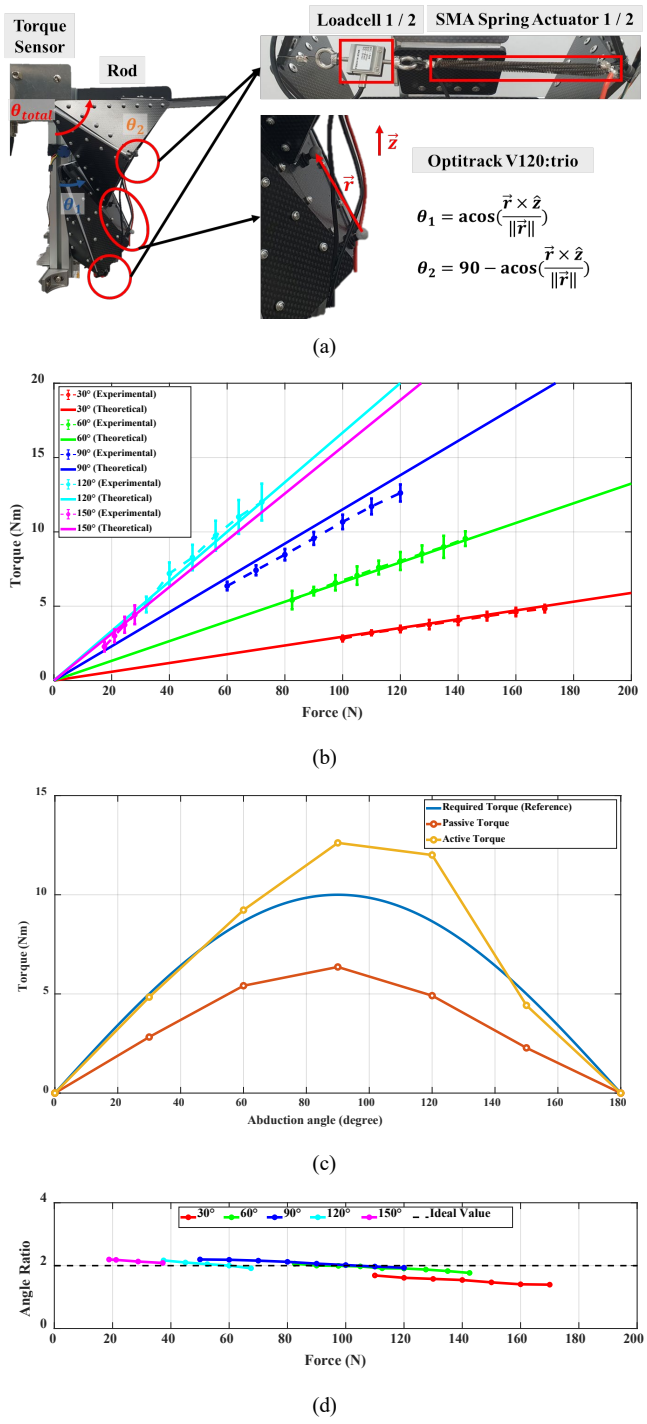


Fig. 7. (a) The test bed for measuring torque output and angle ratio as the input forces to each petal increases. (b) Comparison of the input force and torque output relationship between theoretical data (solid line) and experimental data (dotted line). (c) Relationship between the torque output and abduction angle. (d) Relationship between the angle ratio and input force as the total angle.

when the same forces are exerted on both petals. To validate this, the angle ratio and torque output were measured while applying equal forces to each actuator by increasing the current.

Fig. 7 (a) shows the experimental setup used for performance evaluation. The rod was fixed at the torque sensor with a fixed angle (30°, 60°, 90°, 120°, and 150°). After fixing the total angle ($\theta_{total}$), the same forces were produced to each SMA spring actuator by feedback control using loadcells. Each petal angle was measured using a motion capture camera (Optitrack, V120:trio), and the torque sensor (Dacell, TCN16) was used to measure the torque output due to the force of the actuator. The angles of each petal structure were calculated using the equations as shown in Fig. 7 (a).

The experimental torque output data was compared to the theoretical data as shown in Fig. 7 (b). The input force and torque output at each angle were plotted on x-axis and y-axis, respectively. And the solid line represents the relationship between theoretical actuator force and output torque, the dotted line represents the experimental value, and each color represents the sum of two petal angles, that is, $\theta_{total}$. The results show that the error between the experimental and theoretical data is below 10 %. Also, the maximum torque at 90° is about 12.6 Nm and 6.36 Nm, which is produced actively and passively, respectively, and it is sufficient to assist shoulder abduction as shown in Fig. 7 (c).

Next, Fig. 7 (d) shows the trend of the angle ratio as the input forces ($F_{in}$) of the SMA actuators increase at each total angle ($\theta_{total}$). The angle ratio of the petal mechanism is maintained at 2, with an error of up to 10 % at the most angle. However, in the case of 30°, angle ratio maintains a value of about 1.5, which is less than 2. Additionally, it was confirmed that the angle ratio did not maintain at its initial value but gradually decreased as the input force increased. This is thought to be the result of increased torque applied to the soft hinge as the magnitude of the applied force increases and it undergoes unexpected deformation. However, it was confirmed that even with a significant increase in the force of the actuator, the angle ratio decreased only by around 5 % over 30°. At the abduction angle below 30°, the misalignment error between SHR and proposed mechanism, caused by the small angle ratio, only occurs about few millimeters, so it may be acceptable for assisting shoulder abduction safely.

## III. User Test using Prototype Wearable Robot

### A. Prototype Design Development

To evaluate the assisting performance of the proposed system, a user test was necessary with participants wearing a prototype robot. Therefore, a prototype design of the wearable robot to assist shoulder abduction was developed based on the proposed mechanism as shown in Fig. 8. There are mainly two considerations in fabricating the wearable robot prototype. First, the structure must tightly fit against the body to prevent it from slipping during activation. To achieve this, it is necessary to incorporate an adjustable part in the area where the arm is fixed, allowing for a customized and tight fit for everyone. Also, it is needed to minimize the pain to the user.

Therefore, the supporters were incorporated at the shoulder, arm, and flank to prevent slippage problems. During the working of the mechanism, a gravity is applied to the mechanism and the shoulder supporter ensures that the mechanism remains in place and does not fall. In addition, the use of an adjustment part allows for a secure and customized fit to the individual's body, minimizing any slippage.

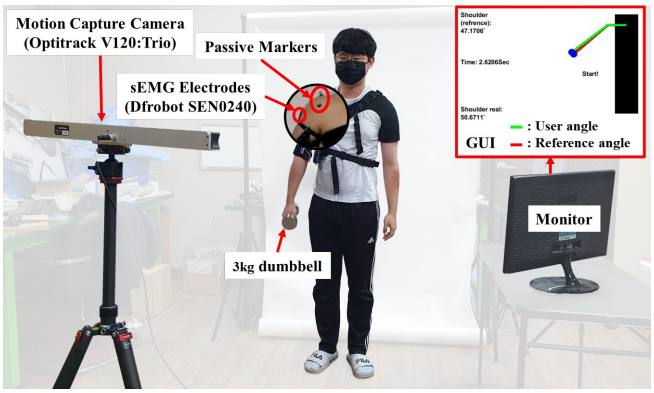


(a)

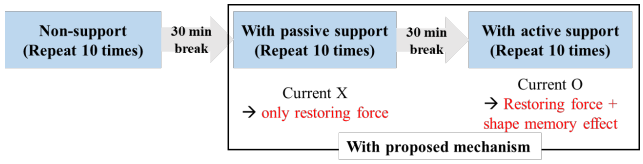


(b)

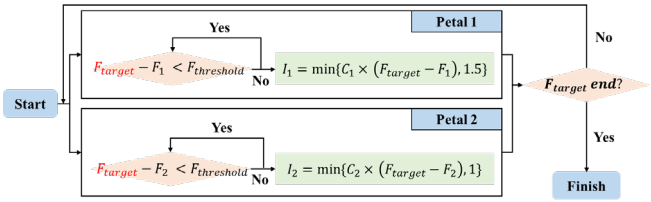


(c)

Fig. 8. (a) The setup, (b) sequence, and (c) block diagram of the control strategy of the user test.

Therefore, soft thermoplastic polyurethane (TPU) 3D printing was used for body-contacting parts such as flank supporter, ensuring a comfortable contact with the body. Moreover, polyethylene (PE) foam tape was used in areas where the pressure is concentrated, effectively reducing any potential discomfort or pain.

## *B. User Test Setup*

To verify the assistive effect of the proposed wearable robot, a user test was conducted. A representative method for confirming muscle activity is to measure surface electromyography (sEMG) signal, and as the muscle becomes more active, the amplitude of the sEMG signal increases. Then, if the assistance of the proposed robot is enough to shoulder abduction, the sEMG signal from the muscle will be decreased. Therefore, sEMG signal of the lateral deltoid, the major muscle of the shoulder abduction, was measured and compared. Also, the trajectory of the GH joint was measured and compared to verify whether the proposed robot assists in following SHR trajectory. This study was approved by the Institutional Review Board at the Korea Advanced Institute of Science and Technology (KH2021-195).

Ten healthy male subjects who had not suffered from any musculoskeletal injuries participated in the user test, and their average age, weight, and height were 26.8 ± 1.9, 172.5 ± 3.1 cm, and 65.8 ± 9.4 kg, respectively. Fig. 9. (a) shows the overall setup of the user test. The sEMG electrodes (DFRobot, SEN0240) were attached at the lateral deltoid muscle and the

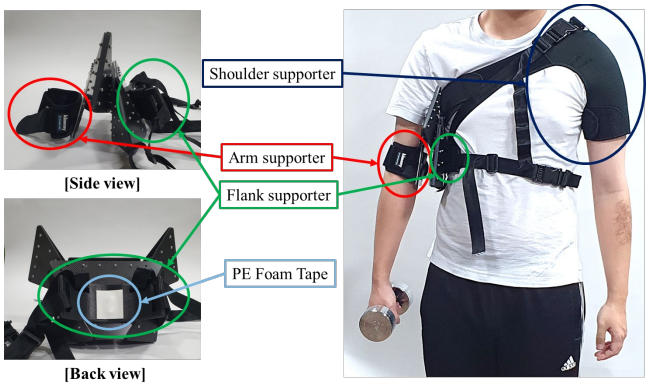


Fig. 9. Development of the prototype wearable robot using proposed mechanism.

passive markers for what attached around the GH joint. The trajectory of markers was then captured using a motion capture camera. Subjects were asked to hold a 3kg dumbbell and proceed with shoulder abduction from 0° to 90° in 5 seconds according to the graphical user interface (GUI) displayed on the monitor. The GUI displayed the reference angle rotating at a constant speed of 18°/s with the real angle of the subject arm, and subjects were requested to follow the reference angle. The subjects requested to repeat the same exercise ten times respectively to ensure reliability.

The sequence of the user test was divided into 3 steps as shown in Fig. 8 (b). First, the subject performed the task without wearing the proposed robot (non-support) and took a sufficient rest at least 30 min to prevent muscle fatigue. Then, the user wears the proposed robot and performs the same task with only the passive support is applied, which operated based on the restoring force of the SMA spring actuator. Then, user will then take a sufficient rest. Finally, the current will be applied to the actuator to provide active support for shoulder abduction. In the case of the active support, using (9) and (10), the required force for each SMA spring actuator to provide assisting torque based on the shoulder abduction angle was determined. If there was a significant difference between the target force and the actuator force, a high current was applied to quickly follow the target force. However, to prevent overheating, maximum current limits were imposed for each actuator. Through this sequence, the performance can be evaluated, considering both active support using energy consumption and passive support relying on the restoring force of the SMA spring actuator.

## *C. User Test Results*

sEMG signals were measured in 1000 Hz using data acquisition (National Instruments Corp., USB-6003) and these data were processed through amplification, band pass filter (BPF) in 20~500 Hz, rectifying, enveloping, and eliminating outliers as shown in Fig. 10 (a). The area of the processed signal was calculated in the time domain. To compare the assistance effect, the average values of the ten exercise trials of non-support, passive, and active support were calculated at each subject, and normalized by setting the standard to 1 for non-support. Fig. 10 (b) shows the average values and standard errors of the normalized sEMG signal data from ten trials of ten subjects, respectively. Every subject, except subject 6, shows that the normalized sEMG values decrease as

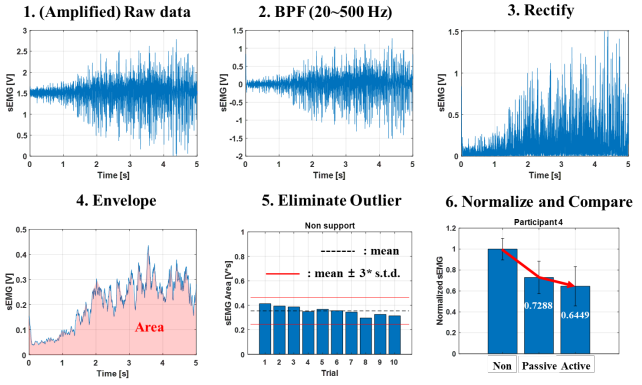


(a)

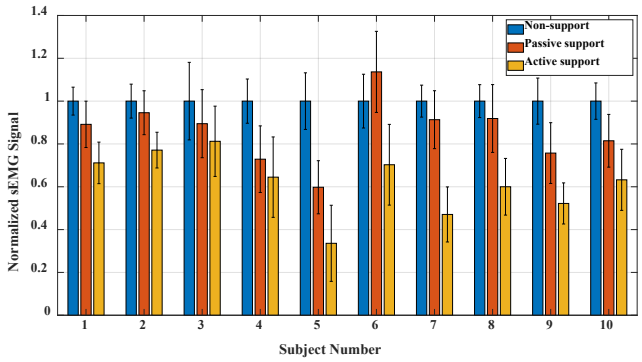


(b)

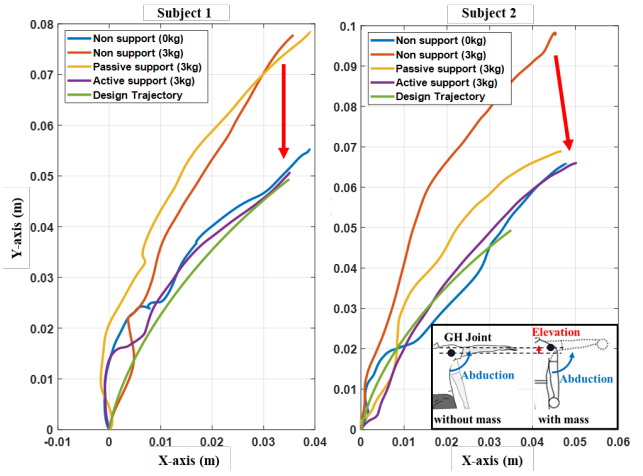


(c)

Fig. 10. (a) sEMG signal process and (b) average values of normalized sEMG signal obtained from ten subjects. (c) Trajectory of GH joint within 5 cases: non-support with and without 3kg dumbbell, passive and active support with dumbbell and designed trajectory of two subjects.

the support goes from non to passive and active. On average, about 14.01 % of the passive support and 37.96 % of the active support were decreased compared to non-support.

Nevertheless, it was necessary to check whether the comparisons between each average data have sufficient reliability. Therefore, one-way ANOVA was performed between each support (non, passive, active support) through the statistic tool (IBM, SPSS Statistics), and the results are shown in TABLE II. When comparing non-support and passive support, it was possible to verify a significant

TABLE II. One-way ANOVA results of user test

| Subject Number | Significance (p-value) | | |
|---|---|---|---|
| | Non → Passive | Non → Active | Passive → Active |
| **1** | 0.007 | 0.000 | 0.000 |
| **2** | 0.311 | 0.000 | 0.000 |
| **3** | 0.291 | 0.029 | 0.465 |
| **4** | 0.000 | 0.000 | 0.238 |
| **5** | 0.000 | 0.000 | 0.000 |
| **6** | 1.000 | 0.000 | 0.000 |
| **7** | 0.099 | 0.000 | 0.000 |
| **8** | 0.216 | 0.000 | 0.000 |
| **9** | 0.000 | 0.000 | 0.000 |
| **10** | 0.000 | 0.000 | 0.014 |
| **Average** | 0.035 | 0.000 | 0.000 |

difference in half of the subjects. However, when comparing non-support with active support, it was possible to verify a significant difference in all subjects, which means that active support sufficiently helps shoulder abduction. Also, the average ANOVA result using total 100 data from 10 subjects shows that the passive and active support confirm the significant differences compared to non-support. In other words, when the users receive active support, it was helpful at a sufficiently reliable level ($p<0.05$).

## IV. Conclusion and Discussion

We proposed a new wearable robot based on the petal mechanism to assist with shoulder abduction. The mechanism was designed to provide sufficient performance, including torque output and ROMs. It ensures safe interaction with humans by minimizing compressive force on GH joint and following SHR. It combines the advantages of the contractive actuator in the direct contraction type and the expandable mechanism in the volume expansion type. The double-petal mechanism mimics the scapula and humerus of the SHR, following each bone. The contraction actuator consists of SMA springs, offering a high power-to-weight ratio and restoring force with lightweight design. The proposed robot can assist shoulder abduction up to 12.6 Nm and 6.36 Nm with and without the energy input, respectively at abduction angle is 90°. Then, user tests with ten healthy men confirmed a significant decrease in muscle activation during active support for all subjects, indicating reliable and effective shoulder abduction assistance.

Using the user test results, we compared GH joint trajectories in 5 shoulder abduction cases: non-support without and with a dumbbell, passive and active support with a dumbbell, and the designed trajectory. This comparison aims to verify if the proposed robot effectively follows the SHR trajectory. Fig. 10 (c) shows two subjects whose GH trajectories conform to the design. They exhibited higher GH joint trajectory during shoulder abduction with a 3kg dumbbell (orange line) compared to without (blue line) in both non-support. It implies that performing shoulder elevation along with shoulder abduction is necessary to generate sufficient torque when using a heavy weight like 3kg dumbbell. However, with sufficient active support, the GH joint trajectory (violet line) follows the natural SHR trajectory

(blue line). Furthermore, this trajectory is similar to the designed trajectory (green line). Therefore, we strongly believe that the proposed robot can provide not only sufficient assisting torque but also safe and stable assistance following the SHR trajectory.

However, there are still several issues that need to be addressed in the future for better performance and usability. In this research, the proposed robot was designed to assist only with shoulder abduction. This means that it cannot assist with shoulder adduction, which is the antagonist movement to shoulder abduction. Due to gravity, the upper limb naturally generates torque in the direction of shoulder adduction. However, in the proposed robot, the shoulder adduction torque is offset by the restoring force of the SMA spring actuators. Therefore, if tasks that require both abduction and adduction movements, such as pulling an object down from a high place in an industrial field, it may rather be a hindrance. To address this, additional actuators for shoulder adduction need to be incorporated to enable assistance in both movements. Furthermore, the current mechanism restricts shoulder flexion/extension, limiting the degrees of freedom (DOF). However, shoulder flexion/extension and internal/external rotation are frequently used in ADL such as eating or drinking, as well as industrial fields. Therefore, in the future, we plan to incorporate a simple origami-based mechanism that does not interfere with other DOF even without the additional actuators.

## REFERENCES


[1] I. Galiana, F. L. Hammond, R. D. Howe, and M. B. Popovic, "Wearable soft robotic device for post-stroke shoulder rehabilitation: Identifying misalignments," *2012 IEEE/RSJ International Conference on Intelligent Robots and Systems*, 2012.

[2] S. Lessard, P. Pansodtee, A. Robbins, J.M.Trombadore, S.Kurniawan, and M.Teodorescu, "A soft exosuit for flexible upper-extremity rehabilitation," *IEEE Trans. Neural Syst. Rehabil. Eng*., vol. 26, no. 8, pp. 1604–1617, Aug. 2018.

[3] K. Hyeon, J. Jeong, C. Chung, M. Cho, S. Hussain, and K.U. Kyung, "Design of a wearable mechanism with shape memory alloy (SMA)-based artificial muscle for assisting with shoulder abduction," *IEEE Robotics and Automation Letters*, vol. 7, no. 4, pp. 10635–10642, 2022.

[4] C. S. Simpson, A. M. Okamura, and E. W. Hawkes, "EXOMUSCLE: An inflatable device for shoulder abduction support," 2017 IEEE International Conference on Robotics and Automation (ICRA), 2017.

[5] R. F. Natividad and C. H. Yeow, "Development of a soft robotic shoulder assistive device for shoulder abduction," in Proc. 6th IEEE Int. Conf. Biomed. Robot. Biomechatronics, pp. 989–993, 2016.

[6] C. T. O'Neill, C. M. McCann, C. J. Hohimer, K. Bertoldi, and C. J. Walsh, "Unfolding textile-based pneumatic actuators for wearable applications," Soft Robot., vol. 9, no. 1, pp. 163–172, Feb. 2022.

[7] A. Ebrahimi, D. Groninger, R. Singer, and U. Schneider, "Control parameter optimization of the actively powered upper body exoskeleton using subjective feedbacks," 2017 3rd International Conference on Control, Automation and Robotics (ICCAR), 2017.

[8] R. Gopura, K. Kiguchi, and Y. Li, "SUEFUL-7: A 7DOF upper-limb exoskeleton robot with muscle model-oriented EMG-based control," IEEE/RSJ International Conference on Intelligent Robots and Systems, pp. 317-322, Oct. 2012.

[9] R. Gopura, D. Bandara, K. Kiguchi, and G. Mann, "Developments in hardware systems of active upper-limb exoskeleton robots: A review," Journal of Robotics and Autonomous Systems, Elsevier, pp. 203-220, Jan. 2016.

[10] D. Park and K.J. Cho, "Development and evaluation of a soft wearable weight support device for reducing muscle fatigue on shoulder," PLOS ONE, vol. 12, no. 3, 2017.

[11] D. Park, S. Toxiri, G. Chini, C. D. Natali, D. G. Caldwell, and J. Ortiz, "Shoulder-Sidewinder (Shoulder-Side wearable industrial ergonomic robot): Design and evaluation of shoulder wearable robot with mechanisms to compensate for joint misalignment," IEEE Trans. Robot., vol. 38, no. 3, pp. 1460–1471, Jun. 2022.

[12] H. Majidi Fard Vatan, S. Nefti-Meziani, S. Davis, Z. Saffari, and H. El-Hussieny, "A review: A comprehensive review of soft and rigid wearable rehabilitation and assistive devices with a focus on the shoulder joint," Journal of Intelligent & Robotic Systems, vol. 102, no. 1, 2021.

[13] M. L. Hansen et al., "Biomechanics of massive rotator cuff tears," The Journal of Bone & Joint Surgery, vol. 90, no. 2, pp. 316–325, 2008.

[14] F. Dyrna et al., "Relationship between deltoid and rotator cuff muscles during dynamic shoulder abduction: A biomechanical study of rotator cuff tear progression," The American Journal of Sports Medicine, vol. 46, no. 8, pp. 1919–1926, 2018.

[15] R. Harbin, *Secrets of origami: The Japanese art of paper folding*. Mineola, NY: Dover Publications, 1997.

[16] M. H. Nizami, Z. A. Shah, Y. Ayaz, M. J. Khan, S. Ali, M. Naveed, K. Akhtar, D. Dancey, and R. Nawaz, "Proximal actuation of an elastically loaded scissors mechanism for the leg design of a quadruped robot," IEEE Access, vol. 8, pp. 208240–208252, 2020.

[17] B. Yu, J. Yang, R. Du, and Y. Zhong, "A versatile pneumatic actuator based on Scissor Mechanisms: Design, modeling, and experiments," IEEE Robotics and Automation Letters, vol. 6, no. 2, pp. 1288–1295, 2021.

[18] A. Pathak, D. Bre, and J. Luntz, "Transformation strain based method for characterization of convective heat transfer from shape memory alloy wires," Smart Mater. Struct., vol. 19, no. 3, Art. no. 035005, Feb. 2010.

[19] J. Jeong, I. B. Yasir, J. Han, C. H. Park, S. K. Bok, and K. U. Kyung, ″Design of shape memory alloy-based soft wearable robot for assisting wrist motion," Appl. Sci., vol. 9, no. 19, Art. no. 4025, Sep. 2019.

[20] J. Jeong et al., "Wrist assisting soft wearable robot with stretchable coolant vessel integrated SMA muscle," IEEE/ASME Trans. Mechatronics, May. 2021.

[21] J. Jeong, C. H. Park, and K. U. Kyung, "Modeling and analysis of SMA actuator embedded in stretchable coolant vascular pursuing artificial muscle," in Proc. IEEE Int. Conf. Robot. Automat., pp. 5641–5646, 2020.

[22] A. Villoslada, A. Flores, D. Copaci, D. Blanco, and L. Moreno, "High-displacement flexible shape memory alloy actuator for soft wearable robots," Robot. Auton. Syst., vol. 73, pp. 91–101, Nov. 2015.

[23] J. Hope and A. McDaid, "Development of wearable wrist and forearm exoskeleton with shape memory alloy actuators," J. Intell. Robot. Syst., vol. 86, no. 3/4, pp. 397–417, 2017.

[24] S. S. Cheng, Y. Kim, and J. P. Desai, "New actuation mechanism for actively cooled SMA springs in a neurosurgical robot," IEEE Trans. Robot., vol. 33, no. 4, pp. 986–993, Aug. 2017.

[25] J. D. Ertel and S. A.Mascaro, "Dynamic thermomechanical modeling of a wet shape memory alloy actuator," J. Dyn. Syst-T ASME., vol. 132, no. 5, pp. 051006-1–051006-9, Sep. 2010.

[26] A. Miriyev, K. Stack, and H. Lipson, "Soft materials for soft actuators," Nat. Commun., vol. 8, Art. no. 596, 2017.

[27] M. Follador, M. Cianchetti, A. Arienti, and C. Laschi, "A general method for the design and fabrication of shape memory alloy active spring actuators," Smart Mater. Struct., vol. 21, no. 115029, Oct. 2012.

[28] Korean Agency for Technology and Standards (KATRi), "8th Size Korea Data", Size Korea, https://sizekorea.kr/human-info/meas-report?measDegree=8 (accessed Feb. 2023).

[29] N. El-Atab, R. B. Mishra, F. Al-Modaf, L. Joharji, A. A. Alsharif, H. Alamoudi, M. Diaz, N. Qaiser, and M. M. Hussain, "Soft actuators for Soft Robotic Applications: A Review," Advanced Intelligent Systems, vol. 2, no. 10, p. 2000128, 2020.

[30] [1] D.-Y. Lee, J.-K. Kim, C.-Y. Sohn, J.-M. Heo, and K.-J. Cho, "High–load capacity Origami Transformable wheel," Science Robotics, vol. 6, no. 53, 2021.